

Spherical Coordinates from Persistent Cohomology

Nikolas C. Schonsheck* and Stefan C. Schonsheck†

Abstract

We describe a method to obtain spherical parameterizations of arbitrary data through the use of persistent cohomology and variational optimization. We begin by computing the second-degree persistent cohomology of the filtered Vietoris-Rips (VR) complex of a data set X . We extract a cocycle α from any significant feature and define an associated map $\alpha : VR(X) \rightarrow S^2$. We use this map as an infeasible initialization for a variational optimization problem with a unique minimizer, up to rigid motion. We employ an alternating gradient descent/Möbius transformation update method to solve the problem and generate a more suitable, i.e., smoother, representative of the homotopy class of α . We show that this process preserves the relevant topological feature of the data and converges to a feasible optimum. Finally, we conduct numerical experiments on both synthetic and real-world data sets to show the efficacy of our proposed approach.

1 Introduction

Representing high dimensional data in a lower dimension through non-linear dimensionality reduction (NLDR) algorithms is a key step in understanding complex data. Different NLDR methods attempt to preserve different key properties of the data, such as global structure [3], local neighborhoods [27], statistical properties [31] or manifold constraints [19], while simultaneously simplifying the representation of the information contained in the dataset [30]. Recently, algorithms that can preserve various topological properties have been of particular interest [5, 8, 9]. In many applications, preserving topological features of data, such as “holes” of various dimensions, is key to downstream tasks including classification, regression, and novel data generation [28]. In this work, we generalize the ideas of de Silva et al. [8] to a higher dimension, producing topologically-invariant spherical parameterizations of data sets as represented by simplicial complexes.

Simplicial complexes are natural generalizations of graphs, capable of encoding higher-dimensional information. From a theoretical standpoint, they are useful in that they provide a “rigid” model for topological spaces that can be represented by a finite sample of points from the space [3]. Moreover, most reasonable spaces can be represented by a simplicial complex up to homotopy equivalence. In applications to data science, their advantages are even more numerous. For instance, whereas graphs contain only vertices and edges, which capture binary relations, simplicial complexes are built from vertices, edges, and their analogs in higher dimensions—namely n -simplices—and can encode relationships between any number of points. Simplicial complexes can also be easily represented on a computer, and there are tractable algorithms and software packages—such as Ripser [2] and Eirene [15]—that can calculate their topological invariants.

In this paper, we develop a method to find spherical parameterizations of simplicial complexes that have nontrivial topology as seen by second-degree cohomology. This method is based on an understanding that instructions for an oriented winding of triangular faces (i.e., 2-simplices) of a simplicial complex X can be extracted from any cocycle in second-degree cohomology. Given a

*University of Delaware, Department of Mathematical Sciences

†University of California Davis, Department of Mathematics, TETRAPODS Institute of Data Science

cocycle and list of faces, we define a variational problem with a unique optimum up to rigid motion. The resulting map $X \rightarrow S^2$ is useful for both data visualization and downstream analysis. In summary, our main contributions are as follows.

- A generalization of the circular coordinates method of de Silva et al. [8] to spherical coordinates.
- A definition of *discrete simplicial harmonic energy* for maps between simplicial complexes and the unit sphere based on oriented winding, or degree.
- A generalized *discrete simplicial spring energy*, based on the energy above, which can be useful for noisy or non-uniformly sampled data including in the 1-dimensional, or circular, case.
- An efficient optimization method for minimizing these energies in both the one and two-dimensional settings.
- A proof that our smoothing procedure preserves the homotopical information encoded by the initial map.

1.1 Related Work

The fundamental idea of this paper—that natural nonlinear coordinate systems for data can be extracted from persistent cohomology—goes back to [8], where the authors recover circular coordinate systems from first-degree persistent cohomology. In more detail, de Silva et al. leverage the natural isomorphism $H^1(X; \mathbb{Z}) \cong [X, K(\mathbb{Z}, 1)]$ given by Brown Representability, and the fact that $K(\mathbb{Z}, 1) \simeq S^1$ to, first, define an initial map $\alpha: X \rightarrow S^1$ that represents a significant topological feature of the data set X . They then determine the “smoothest” such α by finding its harmonic representative in $H^1(X; \mathbb{R})$. Perea [24] strengthens these results using the theory of principal \mathbb{Z} -bundles to design a more efficient and robust method for producing circular coordinates, known as “sparse circular coordinates.”

The work above focuses on one-dimensional persistent cohomology. In this paper, we are interested in what can be obtained from *second* degree persistent cohomology. The reason this is not a straightforward generalization is that in dimension two, Brown Representability gives a natural isomorphism $H^2(X; \mathbb{Z}) \cong [X, K(\mathbb{Z}, 2)]$ and whereas $K(\mathbb{Z}, 1) \simeq S^1$ is amenable to direct calculation, $K(\mathbb{Z}, 2)$ is homotopy equivalent to infinite-dimensional projective space $\mathbb{C}P^\infty$. Perea [23] shows that one can reduce this problem to working in finite-dimensional projective space via dimensionality reduction. However, the question raised in [8] of whether spherical coordinates, i.e., parameterizations $X \rightarrow S^2$, can be obtained from two-dimensional cohomology calculations has remained open thus far. Our results answer this question in the affirmative.

In geometric data processing, defining maps from manifolds (or discrete representation thereof) to spheres has been a popular genre of approach for many problems. Most relevant to this work is that of [12] which defines a discrete version of harmonic energy that can be minimized to find a conformal map from an arbitrary genus-zero 2-manifold (represented as a triangular mesh) to the unit sphere. Other shape processing algorithms have further developed these ideas for quasi-conformal maps [17], non-genus-0 maps [34] and others settings [13, 14]. More recently, [1] developed a shape matching pipeline that utilizes a Möbius transform of the unit sphere to find correspondences between genus-zero 3D shapes. As we will see in Section 4 the group of Möbius transformations will be essential to our smoothing procedure.

In the geometric deep learning community, there has been a recent surge of interest in auto-regressive methods that are topologically informed. Works such as [9, 7, 26, 6] introduce autoencoders with various non-euclidean latent spaces that are useful for problems when the underlying data topology is known and relatively simple. This assumption is too strong for many real-world problems, where the topology is not known *a priori*. In another line of research, [28, 29] and [20]

provide methods for representing data sampled from unknown and arbitrary topological spaces. However, these methods can be sensitive to hyper-parameter tuning, and extracting topological invariants from the trained models is often non-trivial.

Additionally, all of these auto-regressive methods rely on training neural networks with stochastic gradient descent to approximate the desired map(s). In general, the topologies are not guaranteed to be preserved—rather, the authors show that there exist networks that can preserve them and provide numerical experiments to show that the networks often do so. The method presented here, instead, finds the map directly by solving a variational optimization problem and is guaranteed to preserve the homotopy class of the map. Our method does not, however, lend itself directly to novel data generation, but rather to representation learning.

1.2 Acknowledgements

The authors would like to thank Chad Giusti for many helpful discussions, and Jose Perea for an enlightening conversation about the paper. NC Schonsheck’s work is supported by the Air Force Office of Scientific Research under award number FA9550-21-1-0266 and SC Schonsheck’s work is supported by the US National Science Foundation grant DMS-1912747.

2 Persistent Cohomology

In this section, we briefly recapitulate the basics of persistent cohomology. For a more thorough introduction, see [5] and [35]. Another useful treatment is given in [33].

2.1 Background on Persistent Cohomology

Let X be a finite simplicial complex and F a finite field (or, more generally, any commutative ring). For each $n \geq 0$, let $C^n(X; F) = C^n$ denote the F -vector space (more generally, F -module) of *set* maps $X^n \rightarrow F$. That is,

$$C^n(X; F) = \{\text{maps of sets } f: X^n \rightarrow F\} \quad (1)$$

where vector addition and scalar multiplication are inherited from F . Further define coboundary maps $d^n: C^n \rightarrow C^{n+1}$ by

$$\begin{aligned} (d^0 f)(ab) &= f(b) - f(a) \\ (d^1 f)(abc) &= f(bc) - f(ac) + f(ab) \\ (d^2 f)(abcd) &= f(bcd) - f(acd) + f(abd) - f(abc) \\ &\vdots \end{aligned} \quad (2)$$

It is a straightforward check that each d^n is F -linear, allowing us to define the following.

Definition 1. The *degree n cohomology* of the simplicial complex X with coefficients in F is the F -vector space given by

$$H^n(X; F) = H^n(X) = \ker(d^n) / \text{im}(d^{n-1}) \quad (3)$$

In the persistent setting, rather than working with a fixed simplicial complex X , we often consider a filtered simplicial complex X^\bullet , i.e., a sequence of inclusions

$$X^\bullet = X^0 \rightarrow X^1 \rightarrow X^2 \rightarrow \dots \quad (4)$$

where each X^n is a simplicial complex.

Remark 2. Here there is a potential for notational confusion. If X is a simplicial complex, then X^n generally denotes its set of n -simplices. On the other hand, if X^\bullet is a filtered simplicial complex, then X^n refers to a simplicial complex. It will be clear from context which is intended.

Because cohomology is functorial, any diagram as in equation 4 implies the existence of a corresponding diagram in cohomology

$$PH^n(X^\bullet; F) = H^n(X^0; F) \rightarrow H^n(X^1; F) \rightarrow H^n(X^2; F) \rightarrow \dots \quad (5)$$

called the persistent cohomology of X^\bullet . As is evident from equation 5, $PH^n(X^\bullet; F)$ has the structure of a graded F -vector space, which can be thought of as an $F[t]$ -module where t acts via the inclusion maps. In other words, $PH^n(X^\bullet; F)$ is a *persistence module*. Provided F is a field, $F[t]$ is a principal ideal domain (PID), and so if X^\bullet is finite, the Structure Theorem for finitely generated modules over a PID implies that $PH^n(X^\bullet; F)$ can be uniquely decomposed into its *barcode*, i.e., a triple

$$(\text{BC}^n(X^\bullet; F), \beta, \delta) \quad (6)$$

where $\text{BC}^n(X^\bullet; F)$ is a finite set of bars and $\beta, \delta: \text{BC}^n(X^\bullet; F) \rightarrow \mathbb{Z}$ record the birth and death times of each bar. There is also a (nonunique) isomorphism of persistence modules

$$\mathcal{B}: \mathbb{I}_{\text{BC}^n(X^\bullet)} \rightarrow PH^n(X^\bullet; F) \quad (7)$$

where $\mathbb{I}_{\text{BC}^n(X^\bullet)}$ is the *barcode module* for X^\bullet , called an *interval decomposition* of $PH^n(X^\bullet; F)$. The nonuniqueness here arises from choosing a (compatible) basis for each $H^n(X^k; F)$. In this paper, we generally assume that the practitioner has chosen a fixed interval decomposition for any considered persistence module.

2.2 Lifting to Integer Coefficients

In practice, one generally computes persistent cohomology with coefficients in a finite field \mathbb{F}_p . However, our process for defining an S^2 -valued map, below, requires an *integral* cohomology class. Given a simplicial complex X , our strategy for obtaining an element of $H^2(X; \mathbb{Z})$ from an element of $H^2(X; \mathbb{F}_p)$ is the same as that of [8]. In more detail, a straightforward analysis of the long exact sequence associated with the Bockstein homomorphism shows that provided $H^3(X; \mathbb{Z})$ has no p -torsion, any element of $H^2(X; \mathbb{F}_p)$ can be lifted to an element of $H^2(X; \mathbb{Z})$. In practice, given $[\alpha_p] \in H^2(X; \mathbb{F}_p)$, we replace the coefficients of α_p with their corresponding congruence class in the range

$$\{-(p-1)/2, \dots, -1, 0, 1, \dots, (p-1)/2\} \quad (8)$$

and verify that the resultant cochain $\alpha \in C^2(X; \mathbb{Z})$ satisfies the cocycle condition. Hence, $[\alpha]$ represents an element of $H^2(X; \mathbb{Z})$. While, theoretically, this procedure may fail (for instance, if there is p -torsion), we have yet to encounter a real-world example where it does.

3 Obtaining a Map to the 2-Sphere

Suppose X^\bullet is a filtered finite simplicial complex, and that $\rho \in \text{BC}^2(X^\bullet; \mathbb{F}_p)$ has been identified as a significant topological feature. Fixing an interval decomposition $\mathcal{B}: \mathbb{I}_{\text{BC}^2(X^\bullet; \mathbb{F}_p)} \rightarrow PH^2(X^\bullet; \mathbb{F}_p)$

and a parameter δ during the lifetime of ρ , we obtain a cohomology class $[\alpha_p] \in H^2(X^\delta; \mathbb{F}_p)$ which we lift, as in Section 2.2, to a class $[\alpha] \in H^2(X^\delta; \mathbb{Z})$. Letting $X = X^\delta$ for notation's sake, we now describe how to construct a sphere-valued map from $[\alpha]$.

The Brown Representability Theorem gives a natural isomorphism

$$H^2(X; \mathbb{Z}) \cong [X, K(\mathbb{Z}, 2)] \quad (9)$$

where the latter term denotes the set (in this case, group) of homotopy class of maps from X into the Eilenberg-MacLane space $K(\mathbb{Z}, 2) \simeq C\mathbb{P}^\infty$. Thus, the homology class $[\alpha]$ determines a unique homotopy class of map $X \rightarrow K(\mathbb{Z}, 2)$, and the goal now is to lift this to a sphere-valued map. Since there is a canonical inclusion $S^2 \hookrightarrow K(\mathbb{Z}, 2)$, we can phrase this as searching for the dotted map below.

$$\begin{array}{ccc} & & S^2 \\ & \nearrow \tilde{\alpha} & \downarrow \\ X & \xrightarrow{\alpha} & K(\mathbb{Z}, 2) \end{array} \quad (10)$$

In general, there will be obstructions to lifting α on all of X because S^2 has (infinitely) many non-trivial higher homotopy groups. However, since the inclusion $\text{sk}_3(X) \hookrightarrow X$ induces an isomorphism $H^2(X; \mathbb{Z}) \xrightarrow{\cong} H^2(\text{sk}_3(X); \mathbb{Z})$, it is reasonable to instead define a lift from $\text{sk}_3(X)$ which, in fact, always exists. To see this, first note that given a generic 2-simplex φ and integer n , there is a homotopy-unique map $\varphi \rightarrow S^2$ defined by collapsing the boundary of φ to obtain a 2-sphere, then mapping to S^2 via the degree n map. We now define the desired lift $\tilde{\alpha}$.

Definition 3. Let $\alpha \in Z^2(X; \mathbb{Z})$ be a 2-cocycle and fix a basepoint $p \in S^2$. We define the *canonical lift* of α to be the map $\tilde{\alpha}: \text{sk}_3(X) \rightarrow S^2$ defined by mapping each vertex and 1-simplex of X to p and mapping each 2-simplex of X to S^2 as described above. The following shows that this map can then be extended to $\text{sk}_3(X)$.

Proposition 4. The map defined on $\text{sk}_2(X)$ in Definition 3 can be extended to $\text{sk}_3(X)$.

Proof. Let $\sigma = abcd$ be a 3-simplex in X . The map $\tilde{\alpha}$ can be extended to σ if and only if the map from the boundary of σ to S^2 is nullhomotopic. Since the boundary of σ is homeomorphic to S^2 , this map will be determined up to homotopy by its degree (by the Hopf degree theorem) and be nullhomotopic if and only if it is of degree 0. The fact that α is a cocycle guarantees exactly that. To see this, consider the composite below (Figure 1), determined by $\tilde{\alpha}$ on $\text{sk}_2(X)$.

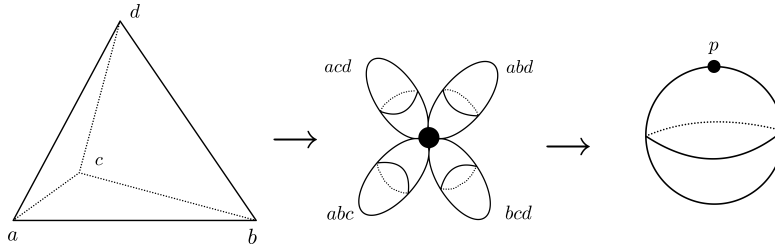


Figure 1: Given a 2-cocycle α , we consider the corresponding map on the boundary of a generic 3-simplex σ .

Let f denote the first map in Figure 1, g the second, and fix an orientation (i.e., an inward or outward facing normal which we denote as $\omega = \pm 1$) of S^2 . We have induced maps on second-degree homology given by

$$\mathbb{Z} \xrightarrow{f_*} \mathbb{Z}_{bcd} \oplus \mathbb{Z}_{acd} \oplus \mathbb{Z}_{abd} \oplus \mathbb{Z}_{abc} \xrightarrow{g_*} \mathbb{Z} \quad (11)$$

The map f_* is given by either $f_*(1) = (1, -1, 1, -1)$ or $f_*(1) = (-1, 1, -1, 1)$, depending on the chosen orientation. In either case, g_* is determined by

$$g_*(1, 1, 1, 1) = \alpha(bcd) + \alpha(acd) + \alpha(abd) + \alpha(abc) \quad (12)$$

and the cocycle condition guarantees that $f^*g^* = 0$. Indeed, we have

$$g_*f_*(1) = \pm(\alpha(bcd) - \alpha(acd) + \alpha(abd) - \alpha(abc)) = 0 \quad (13)$$

Repeating this argument for all 3-simplices of X completes the proof. \square

4 Smoothing the Initial Map

Although we have now obtained a map from a Vietoris-Rips complex on our data to the unit sphere, it is not very useful for visualization or analysis since all of the vertices are mapped to the same point. Next, we describe our procedure for smoothing this initial map to obtain a more desirable representation and prove that this smoothing process preserves the homotopy class of the initial map.

4.1 Harmonic Energy

In order to obtain a useful representation of the data, we define a notion of harmonic energy of a map from an arbitrary 2-simplex to the unit sphere. We minimize this energy across the whole simplicial complex in order to smooth the initial map. Later, we will show that this process preserves the homotopy class of the initial map and results in a more tractable representation of the data the initial map.

Definition 5. For ease of notation, let x be an arbitrary 2-simplex in X^2 . We define the *discrete simplicial harmonic energy* for a map $\alpha: \text{sk}_3(X) \rightarrow S^2$ as:

$$\mathcal{E}_H(\alpha(X)) = \sum_{x \in X^2} \frac{1}{2} \|A(\alpha(x))\|^2$$

where $A(\alpha(x))$ is the area of the spherical triangle to which x is mapped.

Elements $x \in X^2$ that are mapped via the degree 1 or -1 map as in Proposition 4 are assigned an area of 4π (i.e., the whole sphere) and those that are mapped via the degree 0 map are set to 0. Note that a map of degree 0 that collapses all of the vertices to a single point has zero area. Additionally, a triangle with two coincidental vertices has zero area, and therefore zero harmonic energy as well. This energy is a direct generalization of the discrete harmonic energy proposed in [12] in that if our 2-simplex X^2 is in fact a regular, air-tight triangle mesh, then the energies are identical.

A spherical triangle with an area less than 4π can be uniquely identified by three points and its barycenter. (Note that without the barycenter three points on the sphere define two spherically-complementary triangles). Given this information we can measure the sides lengths, a, b, c , and semiperimeter, $s = \frac{1}{2}(a + b + c)$, of the triangle using spherical trigonometry [32]. Finally, we employ L’huillier’s theorem [18] to compute the spherical excess of the triangle. That is: $E(x) = 4 \arctan \left(\tan \frac{s}{2} \tan \frac{s-a}{2} \tan \frac{s-b}{2} \tan \frac{s-c}{2} \right)^{\frac{1}{2}}$. Since we are working on a unit sphere the spherical excess is equal to the surface area of the spherical triangle.

4.2 Spring Energy

In some cases, it is useful to replace harmonic energy with a notion of spring energy so each simplex may have some non-zero rest-state area and so that we can tune a “pull” parameter (i.e., spring constant). Although this introduces additional parameters into the model, we have found that parameter selection is not particularly onerous.

Definition 6. We define the *discrete simplicial spring energy* for a map $\alpha: \text{sk}_3(X) \rightarrow S^2$ as:

$$\mathcal{E}_S(\alpha(X)) = \sum_{x \in X^2} \frac{1}{2} \|k(A(\alpha(x)) - R)\|^2$$

where k is the spring constant, and R is the rest area of the spring.

We will show later in Section 5 that by tuning k and R we can develop better representations of data with nonuniform sampling densities or noise in the barcode. Obviously, setting $R = 0$ and $k = 1$ makes the harmonic and spring energies identical.

4.3 Optimization Routine

Minimizing harmonic (or spring) energy alone is not enough to uniquely determine a map from $VR(X)$ to S^2 since the solution is not unique. The minimums do, however, form a Möbius group [12]. In order to define a unique representation, we first stipulate that the final mapping must have zero-center of mass. This solution is then unique up to rigid motion, which we can fix later during post-processing (see Section 5). Thus, given an initial map $\alpha: VR(X) \rightarrow S^2$, the optimization problem is:

$$\arg \min_{\tilde{\alpha}: VR(X) \rightarrow S^2} \mathcal{E}(\tilde{\alpha}) \quad \text{such that } \tilde{\alpha} \simeq \alpha \quad (14)$$

To solve this problem we use an alternating scheme beginning with the map generated in Section 3. Note this is an infeasible starting point since it is not zero-centered. Moreover, since all of the vertices are mapped to the same point on the sphere, it is not possible to zero center it. First, we decrease the energy by computing the gradient of the energy with respect to the positions of the vertices and performing a step of manifold gradient descent [4]. This spreads the points out, and allows us to approach the feasible region of the zero-center of mass constraint by approximating a Möbius transform which centers the mass afterwards. By choosing the step-size carefully we are able to ensure convergence to a unique minimizer as in [12].

Consider a single spherical triangle with a non-zero area. The negative gradient of the harmonic energy pulls each vertex toward the barycenter. Moreover, the magnitude of the gradient is proportional to the area of the triangle. Then, to perform a step of the gradient update, while remaining on the sphere, we only need to find the geodesic between each vertex and the barycenter. In practice, we compute this direction as the tangent to the geodesic, take a small step in the direction of the gradient in the tangent plane, and then project back to the sphere. So for vertex p , triangle x , and barycenter b , we compute $g = p - b - \langle p - b, p \rangle$, and then the gradient terms:

$$\nabla_{p^\perp, x} \mathcal{E}_H = A(x) \frac{g}{\|g\|_2} \quad \text{and} \quad \nabla_{p^\perp, x} \mathcal{E}_S = k(A(x) - D) \frac{g}{\|g\|_2} \quad (15)$$

Then to compute the gradient of the energy of an entire complex, we simply sum these gradients pointwise over all of the individual triangles x . This process is embarrassingly parallelizable and can be computed extremely efficiently.

For a triangle with non-zero winding (i.e., a triangle which has wrapped around the entire sphere), we have the difficulty that there is not a unique geodesic between the vertex and the barycenter since they are bipolar. Since we have previously defined a positive orientation and negative orientation

for these elements, we can choose a canonical direction of the gradient for one orientation and use its mirror image for the opposite orientation (see Figure 2). After one step in the gradient direction, the triangle will no longer cover the entire sphere and can be treated as those above. Note that a different choice of orientation directions will lead to equivalent results up to some reflection.

Finally, to take perform a step in the direction of the gradient of the energy, we move each vertex in its tangent plane in the direction determined by the gradient, scaled by a step-size parameter, δ_g , and then normalize each point so that they once again lie on the unit sphere. After each gradient step, we update the barycenters of each spherical triangle by finding the euclidean barycenter, normalizing it to the sphere, then choosing the correct pole based on the previous barycenter.

Computing the exact Möbius transform which centers the mass of $\tilde{\alpha}$ is nonlinear and computationally expensive. Instead, following the method of [12], we replace the Möbius transform with an approximation and iteratively update it. First, we compute the current center of mass c and then subtract $\delta_m \alpha c$ from each point. Finally, we project each point back onto the unit sphere using the Gauss map. In order to preserve the triangle orientation, the barycenters are updated identically. Since the initial map α begins with all of the points being mapped to the same basepoint, we compute a few iterations of the gradient descent before beginning the alternating process.

The full algorithm is presented in A

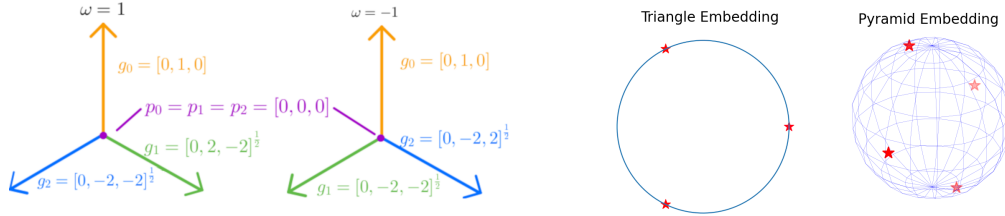


Figure 2: **Left:** Our choice of canonical directions for positive and negative orientations with for triangle with non-zero winding ($\omega = \pm 1$), vertices at $[1, 0, 0]$ and barycenter $[-1, 0, 0]$. The outward normal is chosen to be positive and the inward negative. **Right:** Equilateral Triangle mapped to circle and regular, triangular pyramid mapped to the unit sphere using harmonic energy minimizing maps

4.4 Energy Minimization Preserves Homotopical Information

Recall that the minimization problem begins with a map $\alpha: \text{sk}_3(X) \rightarrow S^2$, i.e., a representative of a homotopy class in $[\text{sk}_3(X), S^2]$ and that the goal is to find a smoother *but homotopic* map $\alpha': \text{sk}_3(X) \rightarrow S^2$. It is crucial, then, that we verify each map produced by our minimization procedure is homotopic to the previous so that we have equivalences

$$\alpha = \alpha_0 \simeq \alpha_1 \simeq \alpha_2 \simeq \cdots \simeq \alpha_N = \tilde{\alpha} \quad (16)$$

through the optimization process. Without this, there would be no topological connection between α , representing a significant feature of the data, and the map produced by our algorithm. Towards proving the string of equivalences in equation 16, we begin with the following.

Proposition 7. *Let X be a space, and suppose f and g are two maps $f, g: X \rightarrow S^2$ from X to the unit sphere in \mathbb{R}^3 . Let $\| - \|$ denote the Euclidean norm and suppose $\|f(x) - g(x)\| < 2$ for all $x \in X$. Then $f \simeq g$.*

Proof. Since $\|f(x) - g(x)\| < 2$ for all $x \in X$, we know that $f(x)$ and $g(x)$ are never antipodal, in which case the straight-line homotopy

$$f_t(x) = \frac{(t-1)f(x) + tg(x)}{\|(t-1)f(x) + tg(x)\|} \quad (17)$$

is well-defined, continuous, and shows $f \simeq g$. \square

Proposition 7 shows that by limiting the distance that the vertices *and barycenter* of each 2-simplex are moved by each gradient descent step, we can guarantee that successive maps in the descent are homotopic, at least up to $\text{sk}_2(X)$. As we observe below, this homotopy can in fact be extended to $\text{sk}_3(X)$.

Proposition 8. *Suppose α_i and α_{i+1} are successive functions in the minimization procedure described in Section 4. If α_{i+1} is obtained from α_i by a gradient descent step, then $\alpha_i \simeq \alpha_{i+1}$ as maps $\text{sk}_3(X) \rightarrow S^2$.*

Proof. It follows from Proposition 7 that α_i and α_{i+1} are homotopic as maps on the 2-skeleton of X . We may assume inductively that α_i extends to a map on $\text{sk}_3(X)$ and the Homotopy Extension Property of the pair $(\text{sk}_3(X), \text{sk}_2(X))$ then ensures that the homotopy between α_i and α_{i+1} can also be extended to the 3-skeleton of X . \square

Lastly, we must show that composing with a Möbius transformation preserves the homotopy class of a map $\text{sk}_3(X) \rightarrow S^2$. We suspect the following is well-known to experts, but record proof here for the sake of completeness.

Proposition 9. *Identifying S^2 with the Riemann sphere (or extended complex plane), any Möbius transformation f is homotopic to the identity.*

Proof. There are a number of ways to see this, but one of the more straightforward is as follows. Identify S^2 with the extended complex plane and represent f as $f(z) = \frac{az+b}{cz+d}$ for $a, b, c, d \in \mathbb{C}$ with $ad - bc \neq 0$. If $c \neq 0$, decompose f into a composition of simpler Möbius functions

$$f_1(z) = z + \frac{c}{d}, \quad f_2(z) = \frac{1}{z}, \quad f_3(z) = \frac{bc - ad}{c^2}z, \quad f_4(z) = z + \frac{a}{c} \quad (18)$$

whence $f = f_4 \circ f_3 \circ f_2 \circ f_1$. For $i = 1, 3, 4$, each f_i is a polynomial on \mathbb{C} that we have canonically extended to $\mathbb{C} \cup \{\infty\}$. It is a well-known fact that the degree of such a function viewed as a map $S^2 \rightarrow S^2$ is equal to its degree as a polynomial. Therefore, $\deg(f_i) = 1$ and so f_i is homotopic to the identity for $i = 1, 3, 4$ by the Hopf degree theorem. Lastly, f_2 represents a rotation S^2 by 180 degrees, so is also homotopic to the identity. Thus, f is a composition of functions each of which is homotopic to the identity, so f is as well. The case $c = 0$ is handled similarly. \square

Together, Propositions 7 and 9 guarantee that our minimization procedure does not alter the homotopy class of the initial map $\text{sk}_3(X) \rightarrow S^2$.

Theorem 10. *Suppose $\alpha = \alpha_0 \rightsquigarrow \alpha_1 \rightsquigarrow \alpha_2 \rightsquigarrow \dots \rightsquigarrow \alpha_N$ is the sequence of maps $\text{sk}_3(X) \rightarrow S^2$ obtained via the minimization procedure described in Section 4. Then $\alpha \simeq \alpha_N$.*

Proof. It follows from Proposition 7 that $\alpha_0 \simeq \alpha_1$. Inductively, suppose that we have shown $\alpha_{i-1} \simeq \alpha_i$. If α_i differs from α_{i+1} by a gradient descent step, then Proposition 7 also shows $\alpha_i \simeq \alpha_{i+1}$. Otherwise, $\alpha_{i+1} = m \circ \alpha_i$ for a Möbius transformation m . In this case, it follows from Proposition 9 that

$$\alpha_{i+1} = m \circ \alpha_i \simeq \text{id} \circ \alpha_i = \alpha_i \quad (19)$$

which completes the proof. \square

4.5 Relation to the 1D Problem

The numerical scheme presented in section 4.3 can also be adapted to map $VR(X)$ to the unit circle S^1 , recovering the original results of [8]. For harmonic energy, it is more efficient to explicitly calculate the harmonic representative as in [8], but formulating the 1D problem is useful for building intuition for the 2D case. Here, the harmonic energy and spring energy for $\alpha: \text{sk}_2(X) \rightarrow S^1$ are given by:

$$\mathcal{E}_H(\alpha(X)) = \sum_{x \in X^1} \frac{1}{2} \|L(\alpha(x))\|^2 \quad \text{and} \quad \mathcal{E}_S(\alpha(X)) = \sum_{x \in X^1} \frac{1}{2} \|k(L(\alpha(x)) - R)\|^2 \quad (20)$$

where $L(\alpha(x))$ is the arc length of $\alpha(x)$, k is a spring constant and R is the spring rest-length. Similar to the set up for the spherical case, we interpret $\omega_\alpha = \pm 1$ as wrapping an edge around the circle in a clockwise ($\omega_\alpha = 1$) or anti-clockwise ($\omega_\alpha = -1$) direction. Since there is a unique harmonic representative of α we do not need to compute Möbius updates, and can instead directly minimize the energy using a first-order scheme. The arguments presented in Section 4.4 show that this scheme preserves the homotopy class of the map, and numerical results in Section 5.1 showcase the usefulness of the spring energy for 1D problems.

5 Numerical Results

Here we present some numerical results on synthetic and real-word data. All experiments were performed in Python using Ripser [2] to compute cohomology classes.

5.1 Synthetic Problems

We begin with a series of illustrative tests on the 1D problem to demonstrate the efficacy of our approach and showcase the difference between the harmonic and spring energy. Figure 3 shows 5 tests of our approach on data sampled from topological circles. The first column shows the original data, the second plots the cocycles computed by Ripser, the third shows the final mapping of the data, and the fourth shows a plot of the circular coordinate (x -axis) vs. an arc length parameterization coordinate of the data. The first test is an evenly sampled circle, for which we recover the original coordinates almost exactly. The second shows a much sparser and more noisily sampled circle. The third row is a trefoil knot, embedded in 3 dimensions, but visualized here in 2. The fourth and fifth rows demonstrate the difference between spring and harmonic energies. We begin with an ellipse in 2D and then embedded it in 50 dimensions and add Gaussian noise. We obtain the cocycles with Ripser then minimize harmonic energy in the fourth row and spring in the fifth. Here we see that the spring energy produces a much more reasonable map since it is able better separate the more densely sampled regions around the ends of the ellipse.

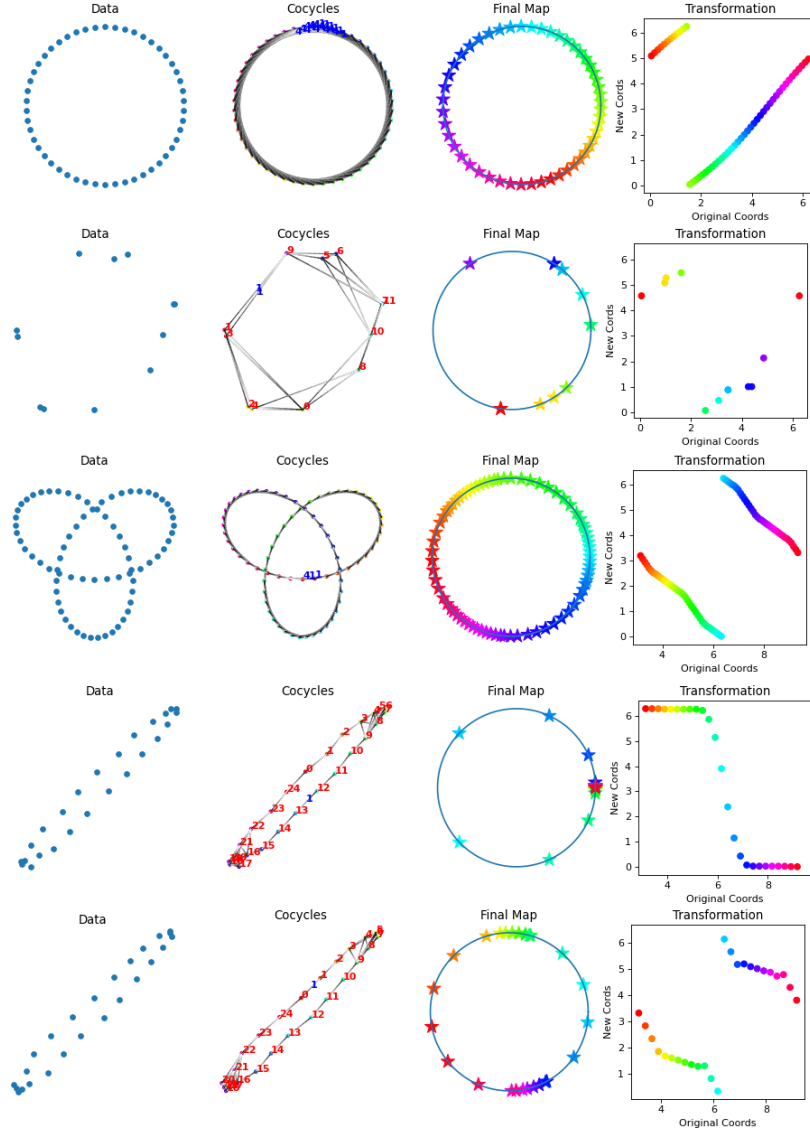


Figure 3: **First Row:** Evenly sampled circle, **Second Row:** Noisy, sparsely sampled circle, **Third Row:** Trefoil knot in 3d (visualized in 2d) with spring energy, **Forth row:** Noisy Ellipse in 5D (visualized in 2D without noise) with harmonic energy, **Last row:** Same as above but with spring energy

Next, we demonstrate our approach to dimension-2 problems. Figure 4 shows a battery of tests. The first column shows the original data. The second column shows the bar codes detected by Ripper and highlights the topological feature that we focus on. The third column shows the final mapping. Finally, the fourth column shows the generated azimuth and elevation coordinates of the initial data versus the final map after alignment. For the ellipsoid cases, we use the paramtools package [16] to generate the sampling. Note that, below, the x and y axes of the “Azimuth” and “Elevation” diagrams are “circular,” so that points very near the top (resp. right) are, in fact, quite close to points near the bottom (resp. left) and vice-versa.

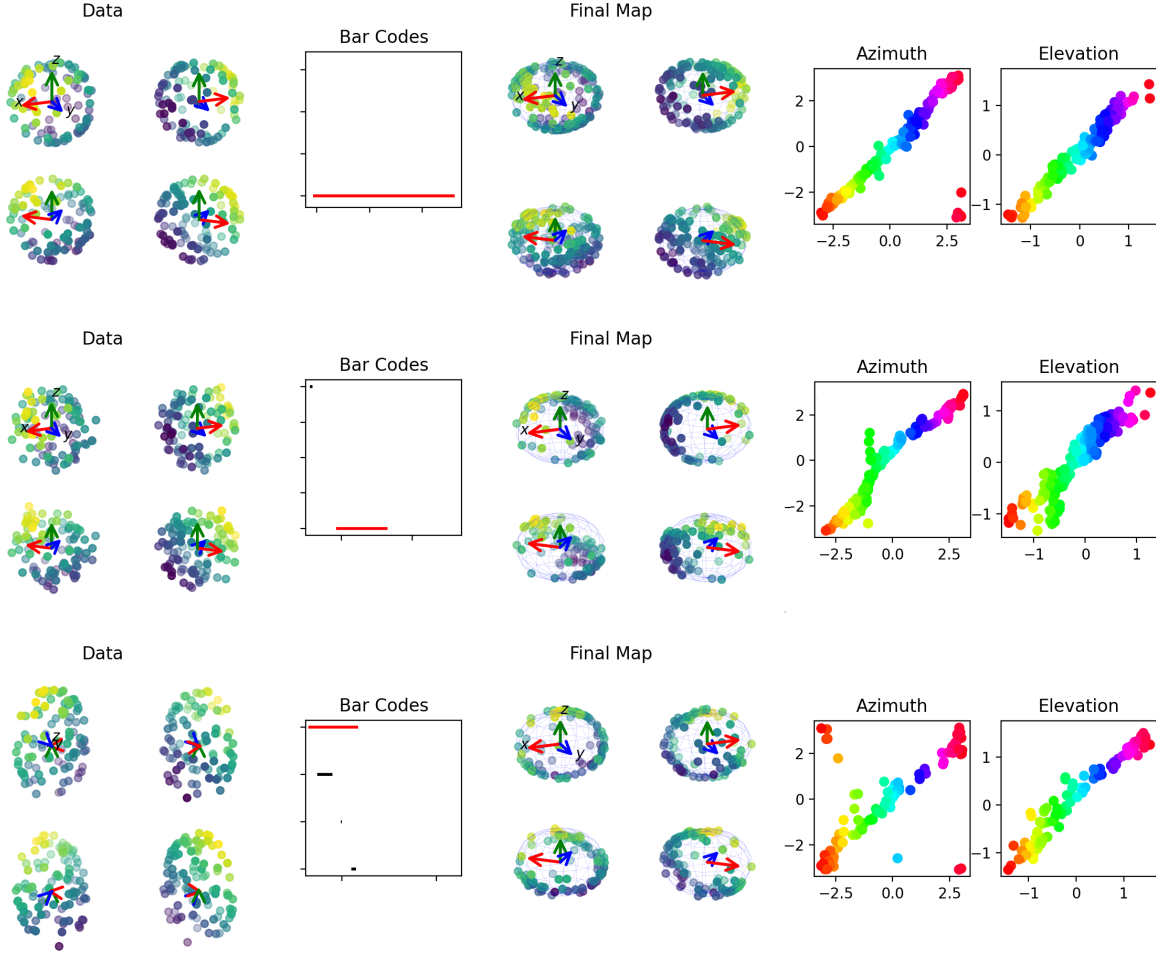


Figure 4: **First Row:** Sphere **Second Row:** Sphere with noise, **Third Row:** Ellipse

5.2 More Complicated Topology

We also illustrate several interesting cases where the underlying topology is not simply a single sphere, but rather some combination of two spherical sub-domains and show how pruning simplexes in a post-process can improve the results by disentangling the subdomains. We begin with two disconnected spheres. Of course, these could be separated in preprocessing, but we delay that in order to build intuition. In the top row of figure 6, we select the feature associated with the red sphere. Even though the spheres are disconnected, the points on the blue sphere still contribute to the zero-center of mass constraint. However, after pruning these points we are able to recover a good representation of each sphere in the last row of the figure. From this observation, we propose a pruning scheme: After completion of the algorithm, if the results are unsatisfactory, we remove all simplexes which have an area less than some threshold (in this case $1e^{-2}$) and apply the minimization procedure to the remaining points.

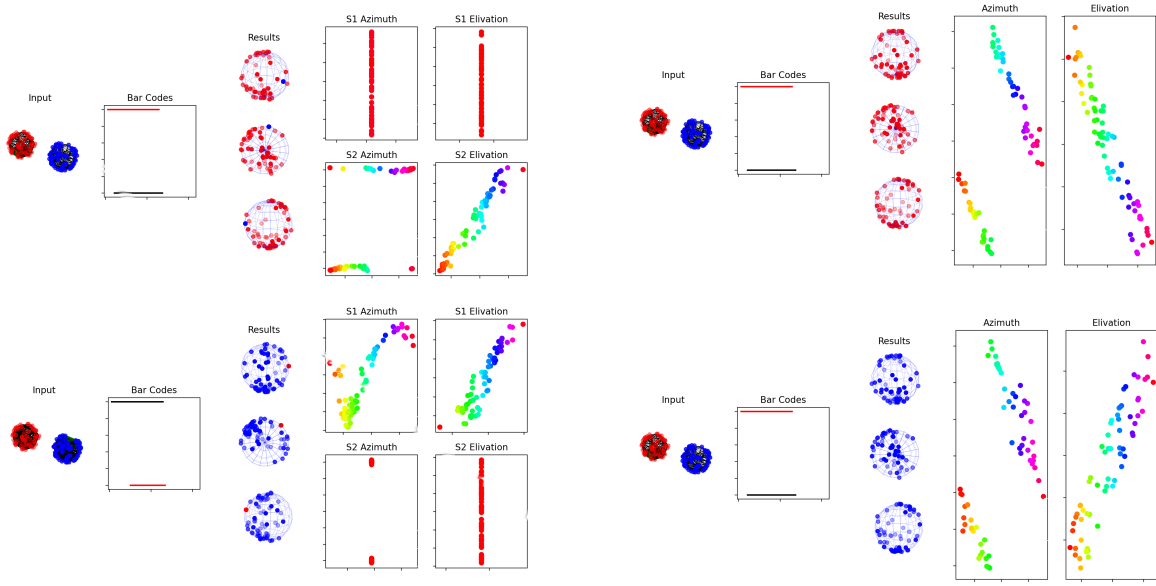


Figure 5: **Columns 1:** Input data. Simplex connections produced by Ripser are shown as black lines. **Column 2:** Barcode with the selected feature highlighted in red. **Columns 3:** Final maps **Column 4-5:** Computed coordinates vs ground truth.

A similar phenomenon appears when applying our algorithm naively to a dataset consisting of points sampled from a wedge of two spheres. Here there are two main topological features, corresponding to the two spheres, that are good candidates for our algorithm. Neither produces a very satisfactory result since the underlying data is non-spherical (left column of Figure 5. Note that in the first case, the chosen feature corresponds to the red sphere, and in the second the chosen one corresponds to the blue sphere. In both of these cases, we see that the points associated with the sphere not chosen are mapped very close to a lower dimensional subspace in the algorithm (a line). In this case, we can apply the pruning scheme explained above. Figure 5 shows the results before and after applying our pruning technique. Although the results are not perfect (note that there are still some red points on the blue sphere and vice versa) we observe that the results are much improved.

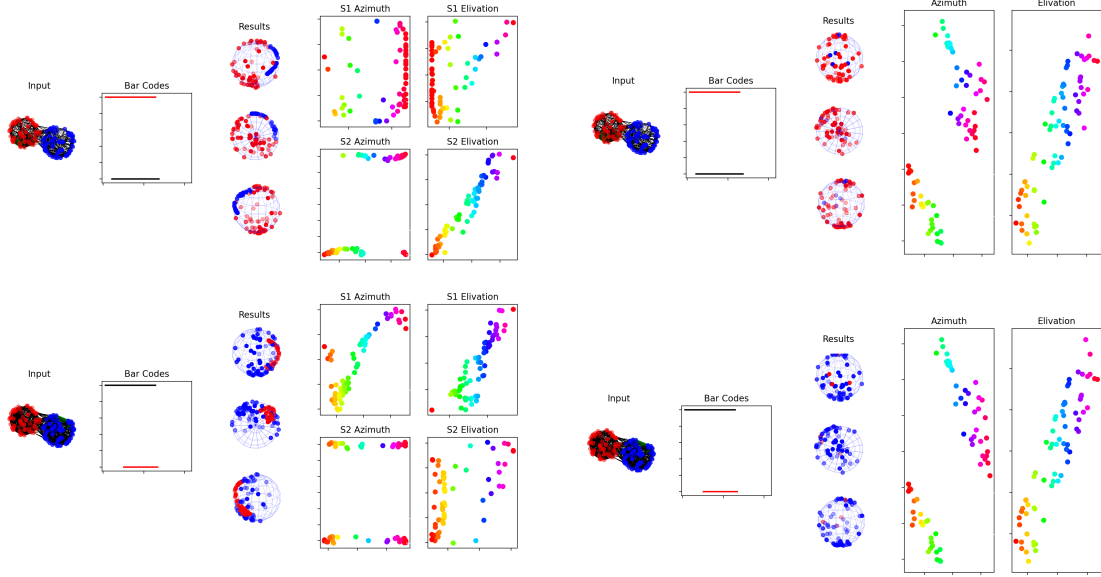


Figure 6: **Column 1:** Input data. Simplex connections produced by Ripser are shown as black lines. **Column 2:** Barcode with the selected feature highlighted in red. **Columns 3:** Final maps **Column 4-5:** Computed coordinates vs ground truth.

5.3 Applied Topological Data Analysis Problems

We begin with our more realistic tests using a 1D example taken from the Columbia Object Image Library (COIL-100) dataset [21]. The dataset contains images of everyday objects (in our case a rubber ducky) photographed from different angles along a single axis of rotation. There are 72 images per object and each image can be represented as a point in \mathbb{R}^{512} . These points can be modeled as coming from a topological circle in \mathbb{R}^{512} . Applying our algorithm to the problem, we are able to closely recover the angle at which each picture was taken. Figure 7 shows the embedding along with the coordinate reconstruction using both harmonic and spring energy minimization. For this case, the harmonic energy minimization did not produce satisfactory results as shown in the left side of Figure 7.

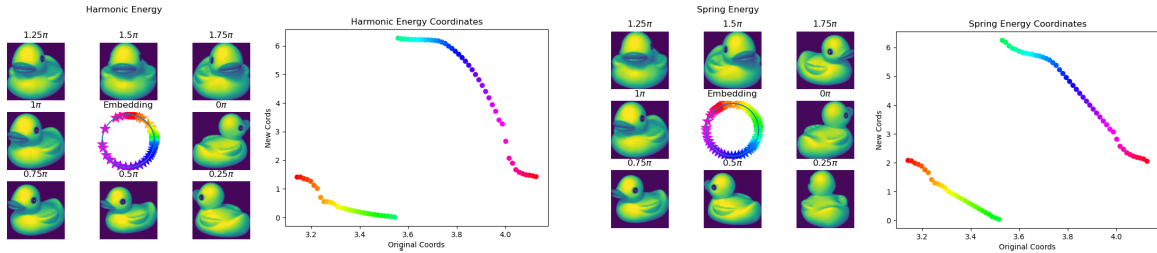


Figure 7: **Left:** The embedding of the Coil-100 duck. Starting with an arbitrary origin, we show the images whose final coordinates differ by $\frac{\pi}{4}$. **Right:** Coordinates of final map vs ground truth coordinates from dataset

We conduct a similar experiment for the 2D problem by rotating an object in 3D. In Figure 8 we show the results of applying our algorithm to a dataset consisting of 200 images of the Stanford

Bunny [25] under random rotations. Although the barcode of the dataset is irregular, by selecting the maximum barcode and using a large enough spring constant we are able to embed the images onto the sphere in a meaningful way.

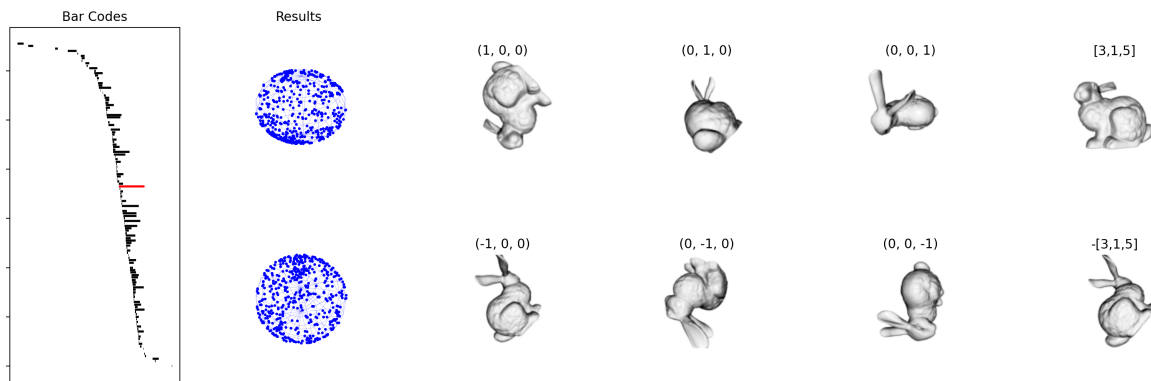


Figure 8: Stanford bunny experiment. In the right 4 columns, we show the images nearest to the point indicated in the subtitle.

We also conduct a synthetic experiment inspired by applications of topological data analysis to neuroscience. It has long been known [22] that certain cells in the hippocampus, called place cells, have spatially localized receptive fields. In other words, they represent one's position during navigation by firing rapidly at specific locations in an environment, while maintaining low activity at all others. Analysis of such data using persistent (co)homology can recover the coarse geometry of the environment itself, e.g., determining if a rat was navigating a circular track, or an open field [11]. Similarly, head direction as encoded by a product of circles can be recovered [10] from neural activity using persistence techniques. We model a variation of this idea: what if place cells were embedded not on, e.g., a circle as a rat runs around a circular track, but rather on a sphere?

We begin by choosing 64 nearly-equally distributed points on the sphere using the Fibonacci lattice. These points serve as sensors for a discrete random walk on the sphere. During the j^{th} step a sensor j measures the distance to walking points as $S_j(x^i) = \exp(-D(x_i, j)) + \mathcal{N}$ where $D(x, j)$ is the distance between x and the j^{th} sensor and \mathcal{N} is random noise. We simulate 25 discrete random walks of length 25 steps and step size $\delta = .1$ on the sphere to generate given a matrix $S = s_{ij}$. Then our goal is to use S to recover the original coordinates of the sensors. Figure 9 shows the coordinate recovery for the cases $N = 0, 0.2, .5$.

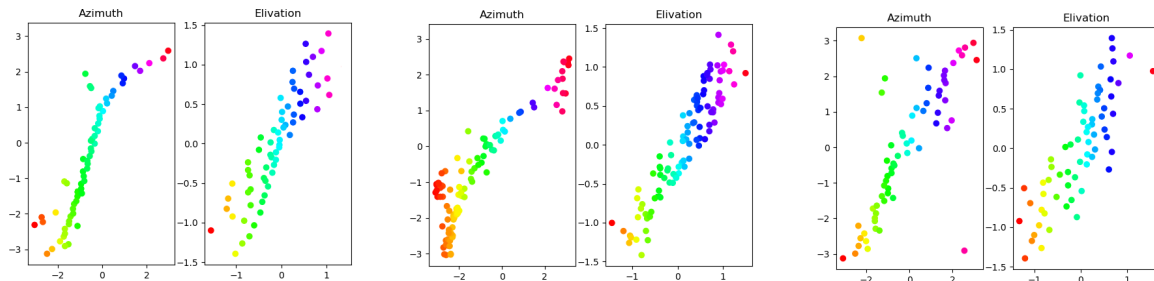


Figure 9: Results from the sensors experiments under different levels of noise. From Right to left the noise values are: $\mathcal{N} = 0, 0.2, .5$

References

- [1] Alex Baden, Keenan Crane, and Misha Kazhdan. Möbius registration. In *Computer Graphics Forum*, volume 37, pages 211–220. Wiley Online Library, 2018.
- [2] Ulrich Bauer. Ripser: efficient computation of vietoris-rips persistence barcodes. *Journal of Applied and Computational Topology*, 2021.
- [3] Mikhail Belkin and Partha Niyogi. Laplacian eigenmaps for dimensionality reduction and data representation. *Neural computation*, 15(6):1373–1396, 2003.
- [4] Silvere Bonnabel. Stochastic gradient descent on riemannian manifolds. *IEEE Transactions on Automatic Control*, 58(9):2217–2229, 2013.
- [5] Gunnar Carlsson. Topology and data. *Bull. Amer. Math. Soc. (N.S.)*, 46(2):255–308, 2009.
- [6] Marissa Connor and Christopher Rozell. Representing closed transformation paths in encoded network latent space. *arXiv preprint arXiv:1912.02644*, 2019.
- [7] Tim R Davidson, Luca Falorsi, Nicola De Cao, Thomas Kipf, and Jakub M Tomczak. Hyper-spherical variational auto-encoders. *arXiv preprint arXiv:1804.00891*, 2018.
- [8] Vin De Silva, Dmitriy Morozov, and Mikael Vejdemo-Johansson. Persistent cohomology and circular coordinates. *Discrete & computational geometry*, 45(4):737–759, 2011.
- [9] Luca Falorsi, Pim De Haan, Tim R Davidson, Nicola De Cao, Maurice Weiler, Patrick Forré, and Taco S Cohen. Explorations in homeomorphic variational auto-encoding. *arXiv preprint arXiv:1807.04689*, 2018.
- [10] Arseny Finkelstein, Dori Derdikman, Alon Rubin, Jakob N. Foerster, Liora Las, and Nachum Ulanovsky. Three-dimensional head-direction coding in the bat brain. *Nature*, 517(7533):159–164, 2015.
- [11] Chad Giusti, Eva Pastalkova, Carina Curto, and Vladimir Itskov. Clique topology reveals intrinsic geometric structure in neural correlations. *Proceedings of the National Academy of Sciences of the United States of America*, 112, 02 2015.
- [12] Xianfeng Gu, Yalin Wang, Tony F Chan, Paul M Thompson, and Shing-Tung Yau. Genus zero surface conformal mapping and its application to brain surface mapping. *IEEE transactions on medical imaging*, 23(8):949–958, 2004.
- [13] Xianfeng Gu and Shing-Tung Yau. Global conformal surface parameterization. In *Proceedings of the 2003 Eurographics/ACM SIGGRAPH symposium on Geometry processing*, pages 127–137, 2003.
- [14] Xianfeng David Gu and Shing-Tung Yau. *Computational conformal geometry*, volume 1. International Press Somerville, MA, 2008.
- [15] G. Henselman and R. Ghrist. Matroid Filtrations and Computational Persistent Homology. *ArXiv e-prints*, June 2016.
- [16] Max Kapur. Param tools, 2020.
- [17] Ka Chun Lam and Lok Ming Lui. Landmark-and intensity-based registration with large deformations via quasi-conformal maps. *SIAM Journal on Imaging Sciences*, 7(4):2364–2392, 2014.

- [18] AJ Lhuillier. Maemoire sur la polyaedromaetrie, contenant une daemonstration directe du thaeoraeme d’euler sur les polyaedres, et un examen de diverses exceptions auxquelles ce thaeoraeme est assujetti (extrait par m. gergonne). *Annales de mathematiques pures et appliquees par Gergonne III*, 1812.
- [19] Leland McInnes, John Healy, and James Melville. Umap: Uniform manifold approximation and projection for dimension reduction. *arXiv preprint arXiv:1802.03426*, 2018.
- [20] Michael Moor, Max Horn, Bastian Rieck, and Karsten Borgwardt. Topological autoencoders. In *International conference on machine learning*, pages 7045–7054. PMLR, 2020.
- [21] Sameer A Nene, Shree K Nayar, Hiroshi Murase, et al. Columbia object image library (coil-100). *Report*, 1996.
- [22] John O’Keefe. Place units in the hippocampus of the freely moving rat. *Experimental Neurology*, 51(1):78–109, 1976.
- [23] Jose A. Perea. Multiscale projective coordinates via persistent cohomology of sparse filtrations. *Discrete Comput. Geom.*, 59(1):175–225, 2018.
- [24] Jose A. Perea. Sparse circular coordinates via principal \mathbb{Z} -bundles. In Nils A. Baas, Gunnar E. Carlsson, Gereon Quick, Markus Szymik, and Marius Thaule, editors, *Topological Data Analysis*, pages 435–458, Cham, 2020. Springer International Publishing.
- [25] François Pomerleau, Ming Liu, Francis Colas, and Roland Siegwart. Challenging data sets for point cloud registration algorithms. *The International Journal of Robotics Research*, 31(14):1705–1711, 2012.
- [26] Luis Armando Pérez Rey. Disentanglement with hyperspherical latent spaces using diffusion variational autoencoders. *Proceedings of Machine Learning Research*, 1:1–4, 2019.
- [27] Sam T Roweis and Lawrence K Saul. Nonlinear dimensionality reduction by locally linear embedding. *science*, 290(5500):2323–2326, 2000.
- [28] Stefan C. Schonsheck, Jie Chen, and Rongjie Lai. Chart auto-encoders for manifold structured data. *arXiv preprint arXiv:1912.10094*, 2019.
- [29] Stefan C. Schonsheck, Scott Mahan, Timo Klock, Timo Cloninger, and Rongjie Lai. Semi-supervised manifold learning with complexity decoupled chart autoencoders. *arXiv preprint arXiv:2208.10570*, 2022.
- [30] Flora S Tsai and Kap Luk Chan. Dimensionality reduction techniques for data exploration. In *2007 6th International conference on information, communications & signal processing*, pages 1–5. IEEE, 2007.
- [31] Laurens Van der Maaten and Geoffrey Hinton. Visualizing data using t-sne. *Journal of machine learning research*, 9(11), 2008.
- [32] Eric W Weisstein. Spherical trigonometry. *From MathWorld—A Wolfram Web Ressource. Available from <http://mathworld.wolfram.com/SphericalTrigonometry.html>*, 2008.
- [33] Hee Rhang Yoon, Robert Ghrist, and Chad Giusti. Persistent extension and analogous bars: Data-induced relations between persistence barcodes, 2022.
- [34] Wei Zeng, Dimitris Samaras, and David Gu. Ricci flow for 3d shape analysis. *IEEE Transactions on Pattern Analysis and Machine Intelligence*, 32(4):662–677, 2010.
- [35] Afra Zomorodian and Gunnar Carlsson. Computing persistent homology. *Discrete Comput. Geom.*, 33(2):249–274, 2005.

A Algorithm

Algorithm 1 Energy Minimization

Require: X^2 , B , $\tilde{\alpha}(X)$, r , tol

Initialize $p = [1, 0, 0]^N$

▷ Begin with all points on basepoint

$i = 0$

while Not Converged **do**

$\mathcal{E} \leftarrow 0$ and $\nabla_{p\perp} \mathcal{E} \leftarrow 0$

for $x \in X^2$ **do**

▷ loop through triangles

$\mathcal{E} \leftarrow \mathcal{E} + E(x)$

for $p \in x$ **do**

$g \leftarrow p - B(x)$

$g \leftarrow g - \langle g, p \rangle$

$g \leftarrow \frac{g}{\|g\|_2}$

$\nabla_{p\perp} \mathcal{E}(p) = E(x)g$

▷ update gradient

end for

end for

$p \leftarrow p - r(\nabla_{p\perp} \mathcal{E})$

$p \leftarrow \frac{p}{\|p\|_2}$

$B \leftarrow \frac{\sum_{p \in x} p}{\|\sum_{p \in x} p\|_2}$

▷ Find barycenters of shifted triangles

if $i \geq 50$ **then**

▷ Begin mass centering after points have spread some

$c \leftarrow \sum_p(p)$

$p \leftarrow p - rc$

$p \leftarrow \frac{p}{\|p\|_2}$

$B \leftarrow B - rc$

▷ Barycenters shift the same as points

$B \leftarrow \frac{B}{\|B\|_2}$

end if

$i++$

end while
